Quantifying CMIP6 model uncertainties in extreme precipitation projections

Amal John, Hervé Douville, Aurélien Ribes, Pascal Yiou

Weather and Climate Extremes 36 (2022) 100435

Contents lists available at ScienceDirect

Weather and Climate Extremes

journal homepage: www.elsevier.com/locate/wace

Quantifying CMIP6 model uncertainties in extreme precipitation projections

Amal John [a,c,*], Hervé Douville [a], Aurélien Ribes [a], Pascal Yiou [b]

[a] Centre National de Recherches Météorologiques, Météo-France, CNRS, Toulouse, France
[b] Laboratoire des Sciences du Climat et de l'Environnement, UMR 8212 CEA-CNRS-UVSQ, IPSL & U Paris-Saclay, 91191 Gif-sur-Yvette, France
[c] Université de Toulouse, France

ARTICLE INFO

Keywords:
Climate change
Precipitation
Uncertainty
Extremes

ABSTRACT

Projected changes in precipitation extremes and their uncertainties are evaluated using an ensemble of global climate models from phase 6 of the Coupled Model Intercomparison Project (CMIP). They are scaled by corresponding changes either in global mean surface temperature (ΔGSAT) or in local surface temperature (ΔT) and are expressed in terms of 20-yr return values (RV20) of annual maximum one-day precipitation. Our main objective is to quantify the model response uncertainty and to highlight the regions where changes may not be consistent with the widely used assumption of a Clausius–Clapeyron (CC) rate of ≈7%/K. When using a single realization for each model, as in the latest report from the Intergovernmental Panel on Climate Change (IPCC), the assessed inter-model spread includes both model uncertainty and internal variability, which can be however assessed separately using a large ensemble. Despite the overestimated inter-model spread, our results show a robust enhancement of extreme precipitation with more than 90% of models simulating an increase of RV20. Moreover, this increase is consistent with the CC rate of ≈7%/K over about 83% of the global land domain when scaled by (ΔGSAT). Our results also advocate for producing multiple single model initial condition ensembles in the next CMIP projections, to better filter internal variability out in estimating the response of extreme events.

1. Introduction

Global climate models provide an increasingly comprehensive representation of the climate system and are used as a primary tool for understanding and projecting changes in climate mean, variability and extremes due to human activities. The Intergovernmental Panel on Climate Change (IPCC) in its sixth assessment report (AR6) has re-estimated an increase in the observed global mean surface temperature of 1.09 °C in 2011–2020 relative to the beginning of the industrial revolution (1850–1900), which can be fully attributed to a human influence (IPCC AR6 SPM Masson-Delmotte et al. (2021)). This anthropogenic global warming is reckoned to have long-term consequences on all components of the climate system, including changes in the daily precipitation distribution. Several generations of multi-model simulations contributing to the Coupled Model Intercomparison Project (CMIP), supported by observational evidence, show that both the frequency and intensity of extreme daily precipitation events have increased over recent decades (Allen and Ingram, 2002; Asadieh and Krakauer, 2015; Scherrer et al., 2016; Karl and Easterling, 1999; Kharin et al., 2013; Min et al., 2011; O'Gorman, 2015). This is also documented in the IPCC special report on Managing the Risks of Extremes Events to Advance Climate Change Adaptation (SREX, Seneviratne (2012)).

In the absence of moisture limitation and of significant dynamical response, the extreme precipitation intensity is expected to increase exponentially with the atmospheric temperature at a rate determined by the Clausius–Clapeyron (CC) relationship. A robust scaling of daily precipitation extremes with global warming across scenarios was confirmed by Li et al. (2020) who found that changes in precipitation extremes follow changes in global warming at roughly the CC rate of ≈ 7%/°C in the latest-generation CMIP6 models. Several studies based on climate model simulations show a future increase of precipitation extremes with temperature at a rate comparable to or higher than the CC rate (Li et al., 2020; Kharin et al., 2007; Pall et al., 2007; Allan and Soden, 2008; Sugiyama et al., 2010; Kao and Ganguly, 2011; Muller et al., 2011). However, wet extremes are not expected to intensify in all regions (Trenberth, 2011; Pfahl et al., 2017).

All these studies either show the multi-model mean or median and have not yet assessed the uncertainties in global CMIP6 projections. A suite of different model projections often exhibits a large spread (Lehner et al., 2020) and can even disagree on a particular region becoming wetter or drier (sign change in the future). Even where there is an overall consensus among the models on the sign of changes in the projected extremes due to a warmer climate, the magnitude

* Correspondence to: DESR/CNRM/GMGEC/CLIMSTAT, CNRM/Météo-France, 42, Avenue Gaspard Coriolis, Toulouse, 31100, France.
E-mail address: john.amal@meteo.fr (A. John).

https://doi.org/10.1016/j.wace.2022.100435
Received 8 October 2021; Received in revised form 9 February 2022; Accepted 10 March 2022
Available online 21 March 2022

of such changes can differ considerably. Though the climate models have improved over recent decades (Wyser et al., 2020; Zelinka et al., 2020), these improvements do not necessarily result in a reduced spread among the projections (Douville et al., 2021). Thus, the main focus of this paper is to quantify the model uncertainties in extreme precipitation projections based on CMIP6 models. We also aim to provide a blueprint on using these projections to identify regions where the projected changes in daily precipitation extremes are consistent with the CC rate and those where they are not.

Changes in extreme precipitation against a backdrop of warming climate arise both due to thermodynamic and dynamic effects (Pfahl et al., 2017). A sub-CC relation or even negative dependence on global mean temperature has been found for precipitation extremes over some regions, especially over the climatologically dry oceanic regions in the subtropics, presumably as a result of decreasing moisture availability and enhanced large-scale subsidence (Berg et al., 2009; Hardwick Jones et al., 2010; Utsumi et al., 2011; Pfahl et al., 2017). But the question of an appropriate choice of temperature for scaling extreme precipitation is still an open question and the available studies differ in scope (Zhang et al., 2019; Schroeer and Kirchengast, 2018; Sun et al., 2021). There is a large-scale warming contrast between the continental landmass and the oceans with certain regions over the ocean experiencing a negligible or limited change in the projected surface temperature. The larger warming observed over land may result in a lower scaling with local mean temperature, which may not be considered as a sub-CC scaling rate (Wang et al., 2017). Any departure from the CC rate can be an indication of a dynamical response which may be either amplified or offset by a thermodynamic response regionally (Pfahl et al., 2017; Sherwood et al., 2010; O'Gorman, 2015). Thus here we explore changes in extreme precipitation simply scaled by either global mean or local surface air temperature changes.

Several studies (Alexander et al., 2006; Tebaldi et al., 2006; Sillmann et al., 2013a,b) have used various indices as a proxy for different features of precipitation extremes. Here we focus on extreme events with typical return periods of 20 years (or 20-year return values, RV20) as estimated from the annual maximum one-day precipitation (RX1DAY). Projected long-period RX1DAY return value changes are larger than changes in mean RX1DAY and increase with increasing rarity (Mizuta and Endo, 2020; Wehner, 2020). Here we did not explore longer (e.g., 50 or 100 years) return periods since the associated uncertainties would be even stronger than for our RV20 estimations due to the limited sampling.

The goal of this study is to assess the uncertainties of projected changes in extreme precipitation based on the multi-model CMIP6 ensemble, to discuss the limitations of assessing the inter-model spread using such ensembles of opportunity, and to highlight the regions where projected changes may not be consistent with the widely used assumption of a Clausius–Clapeyron rate of ≈7%/K (Kharin et al., 2013; Westra et al., 2013; Seneviratne et al., 2021). For this purpose, we use the SSP5-8.5 scenario from 35 CMIP6 models. The total spread in this ensemble is therefore a combination of both model response uncertainty and internal variability. Therefore, we also assess the potential contribution of internal variability to the inter-model spread by analyzing the projected changes of the RV20 in the CanESM5 model with 25 realizations, with the same concentration scenario.

The rest of the paper is structured as follows. We start by introducing in Section 2 the models and methods used in this study. Turning to the results in Section 3, we address the uncertainties in the model projections along with a discussion on the role of internal variability using the ensemble simulations from CanESM5. The role of local versus global temperature scaling is also assessed. Section 4 summarizes the main findings. Other supporting figures and tables are available in the online supplementary material.

2. Data and methods

2.1. Data

Daily precipitation data from 35 global climate models from the CMIP6 repositories (Eyring et al., 2016) are used in this study. We combine the historical simulations (1850–2014) with one shared socioeconomic pathways (SSPs) projections (O'Neill et al., 2016) running from 2015 to 2100. The "end of the road" scenario SSP5-8.5 with the highest emissions is used to get maximum climate change signals and, therefore, better isolate the forced RX1DAY response from internal variability without using large initial condition ensembles (which are only available for a limited number of models). We use the one-model-one-vote approach i.e., without giving any particular weights, although there are inter-dependencies across models (eg Knutti and Masson (2013) and Bador et al. (2018)). For each available CMIP6 model, only one member of the historical and SSP5-8.5 simulations are used — a treatment that is consistent with the recent IPCC AR6, and which ensures that all models are treated equally. As the total uncertainty in the projected changes is the sum of both model uncertainties and internal climate variability, we here also analyze a single model initial condition large ensemble, provided by the CanESM5 model (Swart et al., 2019), with 25 individual members. Hence we can quantify an upper bound for the total uncertainties.

2.2. Climate extreme indices and GEV analysis

We first interpolate the daily precipitation data for each model onto a $1° \times 1°$ grid using a first-order conservative remapping. This allows us to compare multiple models with different resolutions (typically 1–2°). For each model, grid point and year, we calculate the annual maximum daily precipitation (RX1DAY), which is a widely used extreme index defined by the expert group on Climate Change Detection and Indices (ETCCDI) (Karl et al., 1999; Peterson et al., 2001).

We then analyze changes in the return values of RX1DAY, in line with some previous studies of Kharin et al. (2013) and Wehner et al. (2020). To estimate the 20-year return values, we modeled the annual maxima of precipitation at each grid point using a nonstationary Generalized Extreme Value (GEV) distribution using $\log(CO_2)$ as the co-variate for both the location and scale parameters (Coles et al., 2001). The parameters are fitted using the Maximum Likelihood Estimate technique (Easterling et al., 2016). $\log(CO)_2$ is used as a single co-variate since it has long been recognized to dominate the world mean temperature projections (Arrhenius, 1896) and allows us to use a common co-variate for all models without introducing any internal variability (Wehner et al., 2020).

In this study, the GEV estimates are computed by introducing a linear co-variate into the location and the scale parameters while the shape parameter is fitted as constant in time (but not uniform across models and grid cells). In a warming world, all GEV parameters may vary between present-day and future climates, but a time-varying shape parameter would not be meaningful because of high estimate uncertainties due to the limited sampling. This assumption was advocated in recent related studies (e.g., Cooley et al. (2007)) and widely used since then (Kharin et al., 2013; Wehner et al., 2020). In contrast, non-stationary location and scale parameters may further increase the quality of the fitted RX1DAY distribution in some regions. The cumulative distribution function for a non-stationary GEV distribution for a random variable X is:

$$F(x) = \exp\left\{-\left[1+\xi\frac{(x-\mu(t))}{\sigma(t)}\right]^{\frac{-1}{\xi}}\right\} \quad (1)$$

where the co-variate appears linearly in the GEV location parameter as $\mu(t) = \mu_0 + \mu_1 \log(CO_2)$ and in the scale parameter as $\sigma(t) =$

$\sigma_0 + \sigma_1 \log(CO_2)$ while ξ is constant in time. This non-stationary fit is performed for each grid point.

To reduce statistical uncertainty in fitting the GEV distributions, the entire RX1DAY time series from 1850 to 2100 was used for all models. Having fitted GEV distribution, the precipitation extremes of our interest are defined as the 20-year return values. Return values are calculated as the exceedance of the annual extreme with probability p or as the quantiles of a GEV distribution. The changes in the intensity of extreme events can be accordingly estimated for different future periods or periods of different warming levels. Changes in the future (2051–2100) are computed with respect to the historical period (1951–2014), while changes at different warming levels are expressed relative to their intensity during the pre-industrial period (1850–1900).

2.3. Global warming levels

We frame the projections by considering the changes at a specified global warming target of 1.5, 2 and 3 K above the pre-industrial level. Climate sensitivity, or the simulated global mean surface air temperature response to more comprehensive radiative forcings, is different across different models (Vial et al., 2013; Lee et al., 2021). As a consequence, the point in time when specified global warming levels (GWLs) are achieved differs largely across models. Models with higher climate sensitivity reach specified GWLs earlier than others. However, some models may not even reach the highest specified GWL before 2100. The first year when GWLs are reached for the 35 CMIP6 models used in this study under the scenario SSP5-8.5 is shown in the supplementary material (Table S.1). The extreme precipitation statistics are then calculated for each model individually over 21 years, extending from 10 years before and after the "central year". We have used a moving average of 21 years before computing the central year.

2.4. Scaling of extreme precipitation with local and global temperature changes

We scale changes in extreme precipitation (ΔRV20) with both global mean surface air temperature change (ΔGSAT) and local surface air temperature change (ΔT). ΔGSAT is calculated as the difference between the areal mean surface temperatures for the projected period and reference period (cf. Table S1). Similarly, ΔT is estimated as the local change in the climatological surface temperature or the rate of change of mean surface temperature at each grid point for the same periods as above. Instead of considering the linear rate of change ($R_{lin} = \Delta P_{ext}/\Delta T_{surf}$) of the extreme precipitation, we assume a multiplicative rate of change, i.e., $\Delta P_{ext} + 1 = (1 + R_{mul})^{\Delta T_{surf}}$. The multiplicative rate of change is thus calculated as:

$$R_{mul} = (\Delta P_{ext} + 1)^{\frac{1}{\Delta T_{surf}}} - 1, \quad (2)$$

where ΔP_{ext} is the change in precipitation extremes (here, ΔRV20) and ΔT_{surf} is the change in surface temperature (either ΔGSAT or ΔT). Both the linear and the multiplicative rates become approximately equal ($R_{lin} \approx R_{mul}$) when ΔRV20 $\ll$ 1 mm/day. Another important point to note here is that for scaling with local temperature changes we masked the regions where the temperature changes are too small (i.e., ΔT $\ll$1 K) to avoid the infinite scaling while using Eq. (2). The masking is done only for those models which show ΔT $\ll$1 K, while we keep the others so that the results are calculated for the models which project a minimum surface warming.

2.5. Hypothesis testing

We also aim to identify the regions where the change in extreme precipitation may occur at a super-CC rate or sub-CC rate. In the latest IPCC report, Seneviratne et al. (2021) conclude with high confidence that precipitation extremes are controlled by both thermodynamic and dynamic processes, and that warming-induced thermodynamic change results in an increase in extreme precipitation at a rate that closely follows the CC relationship at the global scale. Any departure from the CC rate could therefore indicate an additional large-scale dynamical response. Attribution studies such as Pall et al. (2017) show the local dynamical responses lead to non-CC rates. Small scale dynamical responses such as enhanced convection, orographic lifting in atmospheric rivers, or wind intensification in tropical cyclones, can also induce a non-CC rate of change at the local scale. However, our analysis is only based on coarse resolution global CMIP6 models with parameterized convection so that the dynamical response here does not account for explicit mesoscale changes in the storm dynamics that could also modulate the extreme precipitation response (e.g. Chan et al., 2020). Thus, the large scale dynamics are the only non-thermodynamic mechanisms that can be simulated by these models.

The blueprint we provide in Section 4 will serve as a framework to an extended analysis on this matter. This can provide us with much confidence in the areas that are dominated by warming and those regions where changes in the circulation patterns may also matter. For this, we use a simple hypothesis test, where we identify the regions where, e.g., there is no change, using the 80% confidence intervals we obtained from the multi-model framework. If the targeted R_{mul} (rate of change of RV20 with temperature) does not fall within the confidence interval calculated from the 35 models, we conclude that our hypothesis is rejected. When it comes in the range of the confidence interval, we accept the null hypothesis, and the regions are identified accordingly. To identify the regions with no change, we consider the null-hypothesis R_{mul} = 0%/C, while R_{mul} = 7%/K is used as our second hypothesis to find regions of sub-, super-, or consistent with the CC rate.

3. Results

3.1. Intensification of extreme precipitation

Fig. 1 shows the analysis for the median, 10th, and 90th percentiles along with the uncertainty range, which is, the difference between the 90th and 10th percentiles, of the extreme precipitation changes scaled by both the global mean (ΔGSAT, left panel) and local mean (ΔT, right panel) surface air temperature changes. The extreme precipitation rate as a function of both ΔGSAT and ΔT shows a clear increase in its intensity with respect to the historical period (1951–2014). The global average of the multi-model median changes is 5.0%/K (Fig. 1c) for the scaling with ΔGSAT, while it is 5.3%/K (Fig. 1d) for that of ΔT. These close values are slightly smaller than the CC rate of ≈7%/K , which suggests some negative dynamical influence at the regional scale in increasingly subsiding regions, but also some water limitation in such dry regions. From the maps in Fig. 1c, d, the overall large-scale patterns of change remain similar for both temperature scalings, although changes are a bit more pronounced for the scaling with local temperatures. The largest percentage of increase occurs over the tropical areas followed by the high latitudes for the global temperature scaling. For the local scaling, the largest percentage of changes occurs over the tropics followed by the mid-latitude oceans. The stronger warming over the continental landmass can be a major reason for these differences (Wang et al., 2017). Certain regions over the ocean like the north Atlantic and the southern oceans in Fig. 1c are characterized by moderate to high scaled changes in precipitation extremes, which can be linked to the limited changes in the projected local surface temperatures.

Changes in extreme precipitation with ΔGSAT and ΔT scalings vary substantially across the globe. Over most of the mid-latitude land areas, changes do not strongly depend on the scaling method and exhibit a sub-CC rate of 0–4%/K. Over the subtropics, the assessed rate of change deviates further from the CC rate. In particular, there are high rates (super CC) over the Sahara and the intertropical convergence zone (ITCZ), while the climatological dry areas like the basins of the South

Pacific, the north and the south Atlantic, and the south Indian Ocean are marked by reduced, or even negative, rates of change in the extremes. Again, this deviation from the CC rate (≈7%/K) indicates some other factors apart from the thermodynamic features might be at play. Notably, a remarkable property is the increased multi-model spread over these regions (ref., supplementary material), in line with the less robust dynamical response across global climate models (Pfahl et al., 2017). Large departures, whether it is positive or negative, from the CC rate are associated with a larger inter-model spread, suggesting that these regions may be influenced by less robust changes in atmospheric circulation, possibly related to model-dependent patterns of sea surface temperature anomalies or land–sea temperature contrasts (Douville and John, 2021). Another noticeable feature is the impact of the scaling method over the northern high-latitudes. This is partly linked to the Arctic amplification, where the Arctic region gets warm more than twice as fast as the global average (Cohen et al., 2014).

3.2. Range of projected responses in extreme precipitation

Fig. 1a, b, e and f illustrate the 10th and 90th percentiles of extreme precipitation rates for scalings with with global and local warming. The lower and the upper tails of distribution help us to study the worst possible case scenarios and more importantly quantify the uncertainties. The lower tails of extreme precipitation rates are characterized by large-scale features like the negative scaling over the subtropical oceans in the western continental boundaries for both global and local temperature scaling. It is important to note that these regions are predominantly dry areas due to the descending branches of the Hadley cells. The rest of the globe is marked by very small changes either positive or negative that are very close to zero. However, the 90th percentile maps or the upper tail of the distribution show a strong positive increase in precipitation extremes almost everywhere around the globe. These are consistent with super-CC rates (stippling) for the scaling with global warming and, to a large extent, with local warming. Typical to the local warming scaling, the northern mid- and high-latitude land areas are not stippled. This means that the rate of change in extreme precipitation with local warming is sub-CC over these regions even for the 90% quantiles. Moreover, this is consistent across the three maps in the right panel of Fig. 1b, d, f. This results directly from a larger and consistent local warming over these areas, especially in the Arctic.

Another noticeable result is the zero or low-density stippling over the tropical Atlantic ocean, Southern Europe, Chilean Coast, Continental North America and South Africa in all maps of both global and local temperature scalings (Fig. 1). This implies a sub-CC rate over these areas irrespective of the scaling choice. We speculate that the circulation changes, such as a broadening of the subtropical subsidence region, might be responsible for this (Pfahl et al., 2017). Indeed this kind of extension can effectively replace a low-level moisture convergence zone with a regime with low-level divergence where there is a weaker connection between the projected changes in precipitable water versus temperature.

The bottom panels (g, h) in Fig. 1 show the difference between the 10th and 90th percentile values as simulated by a single realization from 35 CMIP6 models. Large differences between the upper and lower quantiles indicate a substantial spread in the projected extreme precipitation changes. These maps quantify the uncertainties in extreme precipitation response and the pattern is very similar to those of the inter-model standard deviation maps as stated earlier in Section 3.1 (also ref., supplementary material). As clearly depicted in these figures, the spread is larger over tropical areas than the rest of the globe. Particularly, over the tropics, the values are notably large in the regions which are climatologically dry or wet, e.g., the subsidence zones of the Hadley cells, the ITCZ, and the Saharan desert. We also see that the overall pattern of the inter-model spread is similar for both temperature scalings. Table 1 reflects the range of model uncertainty in projected changes in extreme precipitation with respect to both local as well as global warming. It summaries the areal averages of the median, 10%-, 90%- quantiles and their difference for the total (global) area, the global land, and global ocean areas separately. It is clear from this Table that the width of confidence range averaged globally is large, about 10.5%, which is more than the average CC rate.

Table 1
Areal mean values (in %/K) of 10%-, 90%- quantiles and median of the extreme precipitation changes scaled by both ΔGSAT and ΔT over the total global area, global land, and global oceans. The table includes the respective values for both the CMIP6 multi-model changes and CanESM5 multi-ensemble changes.

			10	Med	90	Width (90-10)
Total	GSAT	CMIP6	0.7	5.0	9.5	**8.8**
		CanESM5	3.3	4.8	6.2	**2.9**
	T	CMIP6	0.2	5.3	10.7	**10.5**
		CanESM5	3.2	5.0	6.8	**3.6**
Land	GSAT	CMIP6	1.5	5.8	11.1	**9.5**
		CanESM5	4.3	5.9	7.4	**3.1**
	T	CMIP6	1.0	4.6	9.3	**8.3**
		CanESM5	3.4	4.7	6.0	**2.5**
Ocean	GSAT	CMIP6	0.3	4.6	8.8	**8.5**
		CanESM5	2.9	4.3	5.7	**2.8**
	T	CMIP6	−0.1	5.6	11.4	**11.5**
		CanESM5	3.1	5.1	7.1	**4.0**

Several sources of uncertainty can contribute to this spread. The main source is likely due to different representations of the relevant physical processes and to related biases in the models' climatology of present-day precipitation. Moreover, the non-homogeneous temperature gradient from the equator to the poles and the land/sea temperature differences is also a source of larger uncertainty in the local temperature scaling maps. Another potential source of uncertainty is the internal climate variability which also gets translated differently into the total uncertainty with the use of different temperatures for scaling. We discuss potential contribution of internal variability in the next section.

3.3. Role of internal variability

The spread among the single realizations of CMIP6 projections has been mainly interpreted so far as model uncertainty. Yet, it can also arise from internal variability given the limited sampling. In the case of historical extreme precipitation changes at a multi-decadal time scale, internal variability was shown to be a significant driver due to the cancellation between different external forcings (Nath et al., 2018). To get more insight into this, we analyzed the rate of change in precipitation extremes in the 25-member ensemble of the CanESM5 model, and assess the spread across members (Fig. 2). We consider the large ensemble from CanESM5 as a representative estimate of the internal variability range. It should be noted that CanESM5 is one of the low-resolution CMIP6 models, with moderate skill in simulating global extreme precipitation (Wehner et al., 2020). It is also one of the CMIP6 models with the highest climate sensitivity, but this effect is accounted for by the scaling. The globally averaged median values are thus very close between the CMIP6 ensemble and the CanESM5 ensemble for both scaling with ΔGSAT and ΔT (Table 1).

Fig. 2 shows the same diagnostics as in Fig. 1, but we see an obvious visible difference between them along with a few matching large scale patterns. For instance, the rates of change for both ΔGSAT and ΔT match over the climatologically dry regions like the north and south tropical Atlantic oceans as well as over primarily wet regions like the inter-tropical convergence zone. Furthermore, the regions like North American inland, Europe and Eurasia, Chilean Coasts, and South Africa are marked by a sub-CC rate of change with both temperature scales, likewise in Fig. 1. Another noticeable result here is the changes in the

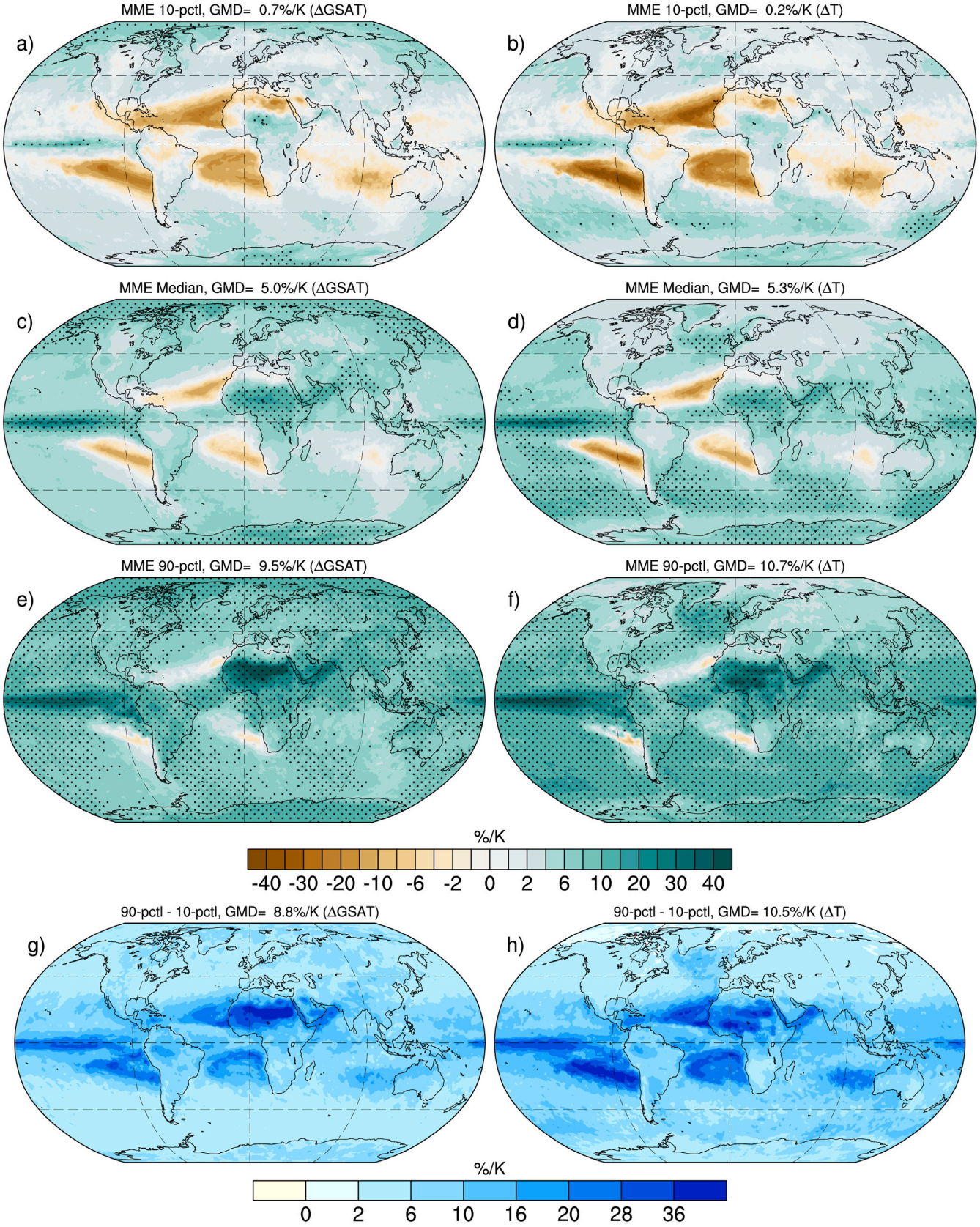

Fig. 1. Projected relative changes (%/K) in 20-yr return values of RX1DAY scaled by both global mean surface temperature change (ΔGSAT in K, left panel) and local mean surface temperature change (ΔT in K, right panel). The changes are calculated for the future period of 2051–2100 relative to the historical period of 1951–2014 using the SSP5-8.8 scenario. (a),(b) show the 10% quantile maps, (c),(d) show the median maps and (e),(f) show the 90% quantile maps, calculated from the CMIP6 multimodel ensemble. The bottom panel shows the width of the confidence range of extreme precipitation, computed as the difference between the 90% and 10% quantile maps. Stippling highlights the grid cells where the rate of change is more than 7%/K for respective scalings with ΔGSAT (left panel) and ΔT (right panel). GMD denotes the global mean differences. (For interpretation of the references to color in this figure legend, the reader is referred to the web version of this article.)

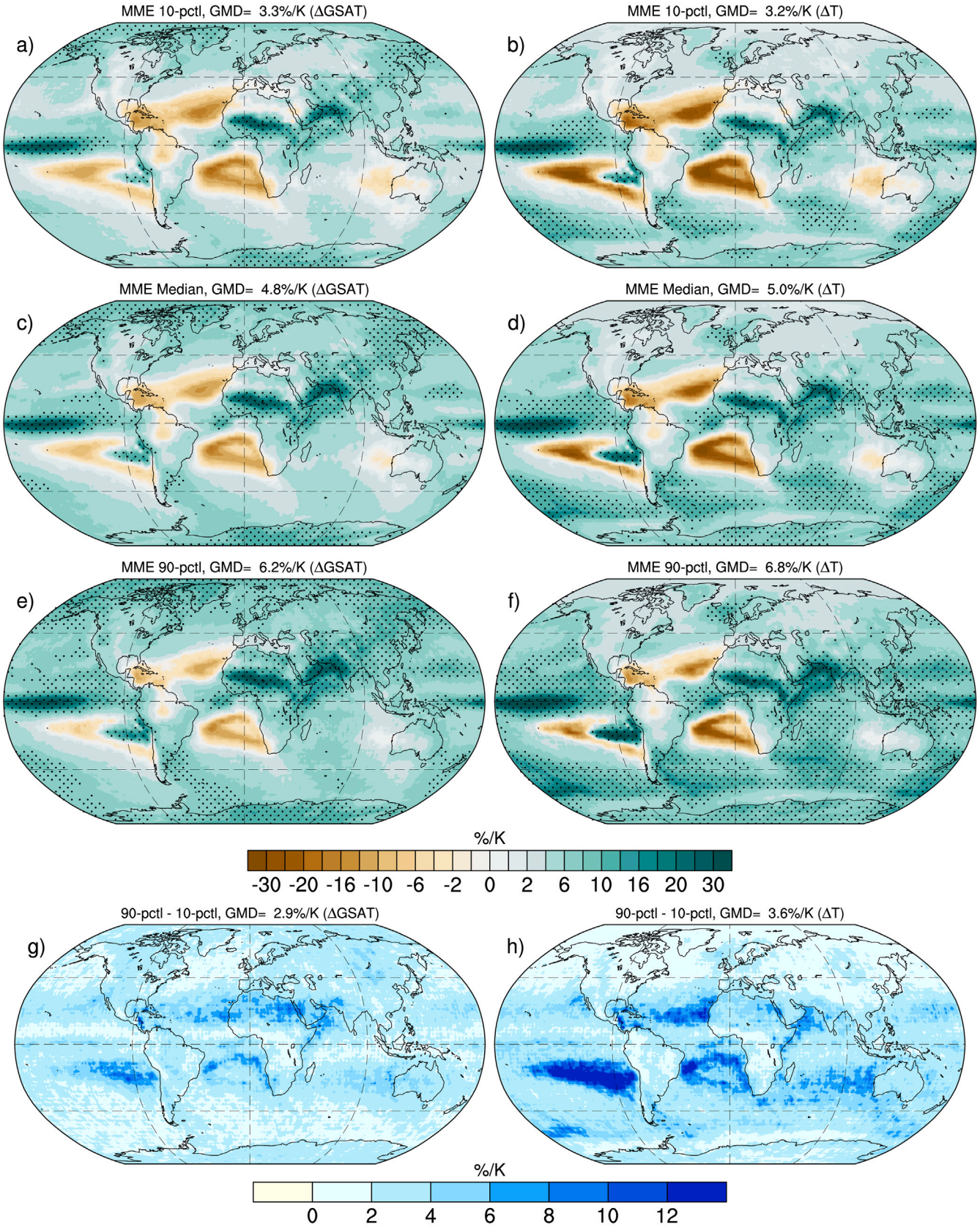

Fig. 2. Same as Fig. 1, but for the ensemble of 25 individual members of CanESM5 model. (For interpretation of the references to color in this figure legend, the reader is referred to the web version of this article.)

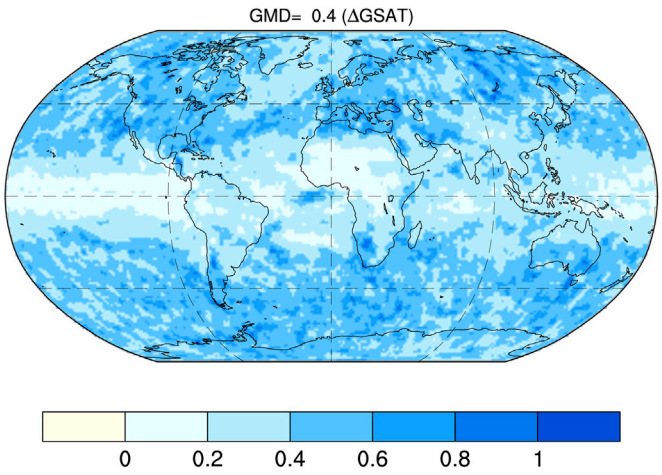

Fig. 3. Ratio of the width of confidence range of extreme precipitation in large ensemble CanESM5 to the CMIP6 multi-model ensemble. The result shown here is for scaling with global mean surface temperature change (ΔGSAT).

areas that are stippled. CanESM5 shows areas of super-CC (>7%/K) even for the 10th percentile maps which are not observed in the CMIP6 ensemble. While for 90th percentile maps we see a decrease in the regions that are super-CC rated. The range of uncertainties (2.9%/K for ΔGSAT and 3.6%/K for ΔT) across the CanESM5 ensemble members is evidently less than that across the CMIP6 models. The total uncertainties depicted in Fig. 2 (bottom panel) is just the result of internal variability. Table 1 again summarizes the mean value of median, 10%-, 90%- quantiles and their difference for the total (global) area, the global land, and global ocean areas separately.

The evidenced range of uncertainty for the large ensemble of CanESM5 suggests that internal variability can contribute significantly to the total uncertainty of extreme precipitation rates, when estimated from one single simulation, even in a very high emission scenario. Fig. 3 depicts the ratio of the width of the confidence range (the difference between 90% and 10% quantiles) of the CanESM5 large ensemble to that of the CMIP6 cross model ensemble. We clearly see that for mean extreme precipitation rates scaled by global mean surface temperature, internal variability alone can induce a range of response about half as large as the CMIP6 multi-model spread (global average of ≈40%). For the high- and mid-latitude regions, internal variability is even larger and explains a range of response ≈75% (darker shades of blue) as large as the total uncertainty. These regions exhibit a low to moderate increase in the percentage response of the extreme precipitation (as shown in Figs. 1, 2) which explains the strong influence that internal variability may have on the extreme precipitation signals. However, throughout the equatorial belt and the adjacent tropical areas, we see a rather less but non-negligible contribution from internal variability. Interestingly, most of these regions fall along with the average position of the ITCZ, which is characterized by high values of extreme precipitation changes. Here, model uncertainty is very likely the major contributor to the assessed inter-model spread, whereas internal variability only contributes to about 0%–20% but is still potentially significant.

Overall, these results suggest that internal variability contributes substantially to the assessed uncertainty (i.e., the width of the 80% confidence range) reported in Fig. 1. As a consequence, modeling uncertainty alone is probably less than shown in Fig. 1. Filtering out internal variability could be done by using multiple members for each CMIP6 model involved — but such data are not available for all models so far.

3.4. Sensitivity of precipitation extremes at different global warming levels

Fig. 4 provides analyzes of the 10%- and 90%- quantiles of global climate sensitivity of RV20 in the CMIP6 ensembles at GWLs of 1.5 K, 2 K, and 3 K respectively. The median changes (figure not shown) relative to the preindustrial period for all GWLs are close to the CC rate of ≈7%/K. Not surprisingly, globally these scaled rates of change in precipitation do not appear to depend on the selected GWL. There is only a slight difference of 0.7%/K in the average multi-model median as the GWL is increased from 1.5 K to 3 K possibly due to a non-linear response in some models (e.g., Pendergrass et al. (2019) based on a CMIP5 model), or just a sampling uncertainty. A notable observation as summarized in Table 2 is that the inter-model uncertainty range tends to decrease as the GWL increases. The lower-tail of the extreme precipitation rates shown by 10th percentile maps for the three GWLs (Fig. 4 left panel) reveals a very small decrease in the average negative precipitation rate values from 1.2%/K (+1.5 K) to 1.1%/K (+2 K) and to 1.0%/K (+3 K). Also, as seen from the right panel of Fig. 4, the upper-tail of the distribution or the 90th percentile maps show that the upper bound of extreme precipitation rates move closer to the median value from 14.9%/K (+1.5 K) to 13.6%/K (2 K) and 12.1%/K (3 K). This reduced uncertainty for higher GWLs is consistent with the expected contribution of internal variability. At lower GWLs, the forced response remains limited, and the additional noise resulting from internal variability is proportionally larger. This finding provides support for investigating changes in extreme precipitation at high GWLs. Moreover, we notice that the uncertainty at +3 K GWL remains larger than that reported in Fig. 1. Again, this is consistent with a smaller contribution of internal variability in Fig. 1 compared to a +3 K GWL — consistent with the fact that SSP5-8.5 leads to global warming higher than +3 K in most CMIP6 models, and that estimating changes over a longer period (50-yr in Fig. 1, vs 20-yr for GWLs) leads to better filtering of internal variability.

Table 2
Areal mean values (in %/K) of 10%- and 90%- quantiles of the extreme precipitation changes scaled by ΔGSAT over the total global area, global land, and global oceans for three target global warming levels of 1.5, 2, and 3 °K.

		10	Med	90	Width (90-10)
Total	1.5 K	1.2	6.5	14.9	**13.7**
	2 K	1.1	6.2	13.6	**12.5**
	3 K	1.0	5.9	12.0	**11.0**
Land	1.5 K	2.0	7.5	19.3	**17.4**
	2 K	1.9	7.2	17.3	**15.4**
	3 K	1.8	6.8	14.8	**13.0**
Ocean	1.5 K	0.8	6.0	12.9	**12.1**
	2 K	0.8	5.8	12.0	**11.2**
	3 K	0.6	5.4	10.8	**10.2**

3.5. Regions of hypothesis tests

Using a simple hypothesis test as described in Section 2.5, we classified the global areas into three categories. Here we have considered two general hypotheses — (H_0) extreme precipitation does not change with global warming, and (H_1, H_2) the change in extreme precipitation follows the CC rate of ≈7%/K for ΔGSAT and ΔT scaling, respectively. Fig. 5 shows the regions categorized accordingly to our hypotheses. Red and blue colors are regions where the hypothesis is rejected while yellow represents regions where the hypothesis is accepted. It is important to notice that accepting a hypothesis does not mean that this hypothesis is true. It rather means that the hypothesis is plausible, i.e., there is not enough evidence to reject it.

Fig. 5 a shows the regions all over the globe where the rate of precipitation change to ΔGSAT is consistent with ≈0%/K (i.e., no significant change, yellow color). We see that the regions for which H_0 cannot be rejected are limited and these are especially over the global oceans. It is to be noted that over these regions the median values of the projected precipitation changes are consistently low and close to zero. The same results are found for the local temperature scaling (with a correlation ≈99%). Over these regions, the cohort of

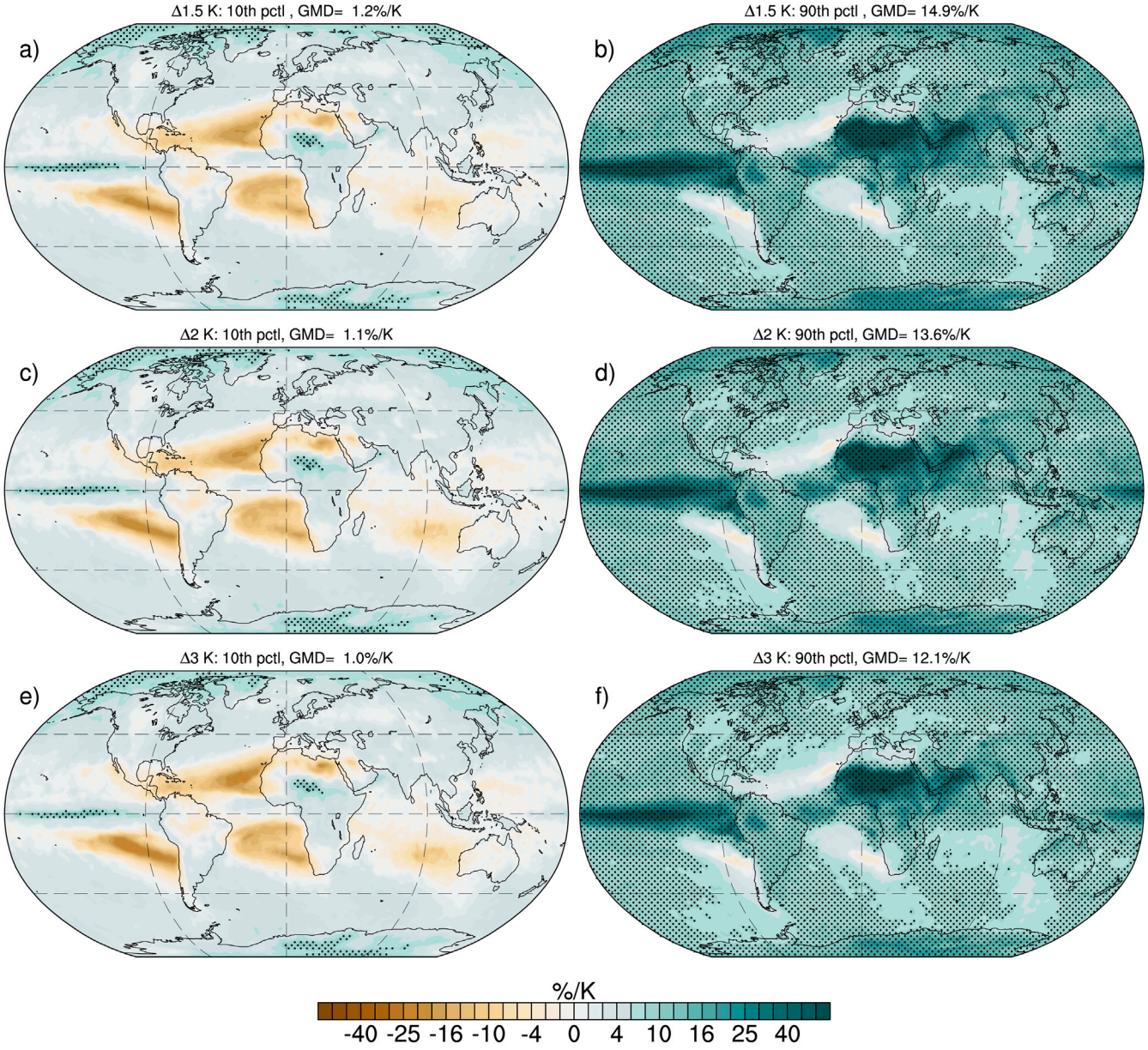

Fig. 4. Projected relative changes (%/K) in 20-yr return values of RX1DAY scaled by global mean surface temperature change (ΔGSAT in °K) at global warming levels of 1.5, 2 and 3 °K above the preindustrial (1850–1900) average values. The left panel shows the 10% quantile maps and the right panel shows 90% quantile maps for the CMIP6 multimodel changes. Stippling marks the grid cells where the rate of change is more than 7%/K. GMD denotes the global mean differences.

CMIP6 models does not provide robust evidence that global warming will intensify extreme precipitation. While the small patches of red colored regions over subtropical ocean west to the continents indicate that the hypothesis is rejected but the changes are negative. Another notable feature over the yellow and red colored regions is the similarity of negative scaling the Fig. 5a to the patterns of negative dynamic contribution as observed in figure 3 of Pfahl et al. (2017) for the CMIP5 models. This implies a consistency between the CMIP5 and CMIP6 projections of extreme precipitation, possibly for a common reason, perhaps, a less robust dynamical response. The negative dynamic factors may perchance responsible for keeping the extreme precipitation not to increase at large as it does with moisture increase in the rest of the globe. Remarkably, there is no land region where extreme precipitation is robustly expected to decrease in response to global warming.

Fig. 5b, c shows the regions where the hypotheses H_1, H_2 are accepted or rejected. Both H_1 and H_2 are used for identifying the regions where the extreme precipitation changes are consistent with the CC rate of ≈7%/K with respect to ΔGSAT and ΔT respectively. These maps can be used as a blueprint to identify the regions which are consistent with the CC rate and those which are not. The first outcome is that a vast majority of places on Earth, about 83% of the global land area, are expected to undergo a change in extreme precipitation that is consistent with the CC rate, particularly with the ΔGSAT scaling. This does not mean that these regions will experience a change of exactly +7%/K. It means that, over these regions, the expected change in prceipitation extremes is not robustly sub-CC or super-CC, i.e., not inconsistent with CC. The majority of regions that follow a sub-CC rate of change for both temperature scalings are over the oceans, especially at the western continental boundaries, which are climatologically dry regions. A few continental regions like the North American continent, South and Central Eastern Europe, Chilean Coast, South Africa and South Australia are also marked by the sub-CC rate for both scaling temperatures. There are also patches of consistent super-CC rates over the equatorial Pacific and the Sahel region. Scaling with two different

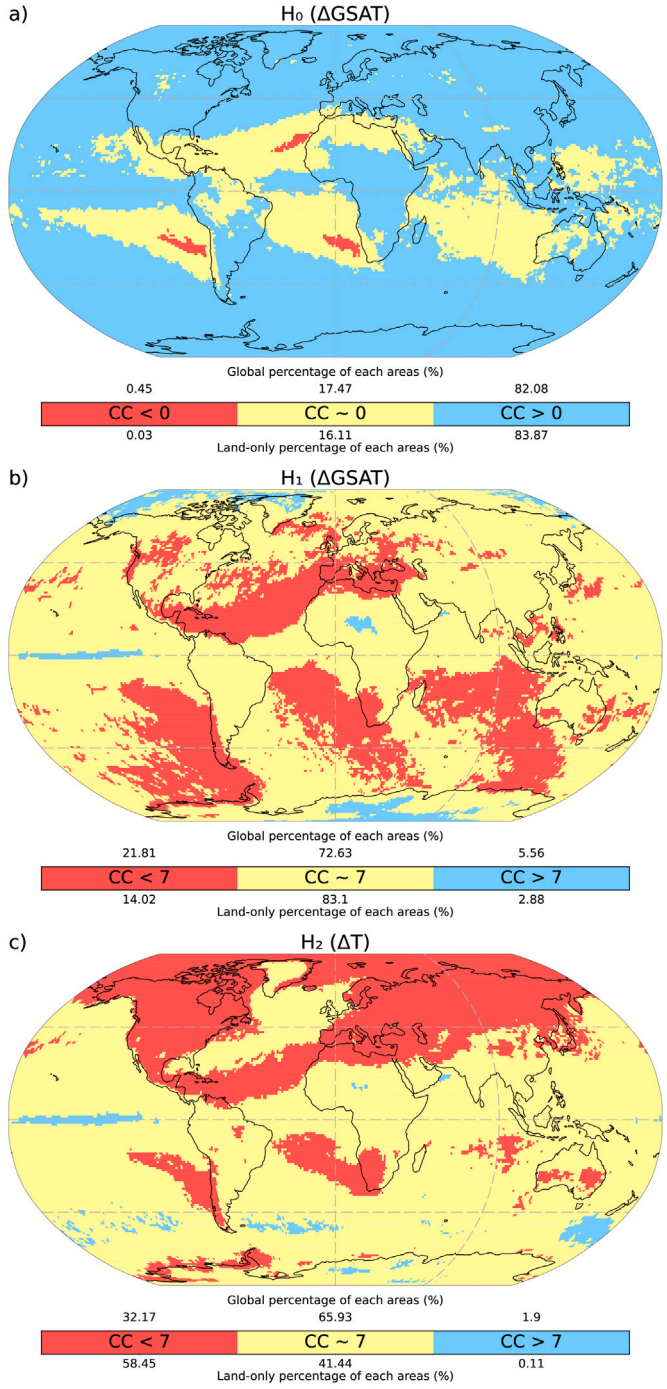

Fig. 5. Global maps of confidence areas (80% confidence interval) for the CMIP6 using 35 individual models with a single realization. The maps show where the rate of extreme precipitation changes is consistent with constant rates of ≈0%/K or ≈7%/K. Red color denotes the regions where the changes are always less than the constant, yellow denotes areas where the constant falls within the confidence interval and blue denotes areas where the rates are always greater than the constant. Map (a) shows the areas where the rate of changes in extreme precipitation remains unchanged or consistent to 0%/K when scaled with ΔGSAT. Maps (b), (c) show the global areas where the rate of changes are consistent with the CC rate of ≈7%/K with respect to ΔGSAT and ΔT. The values on top of colorbar show the percentage of each colored area over the global land surface, while the values at the bottom indicate the same over the total global surface. (For interpretation of the references to color in this figure legend, the reader is referred to the web version of this article.)

temperatures displays different areas of consistency with CC especially over the high Northern latitudes. The map for the local temperature scaling shows a significant increase in the sub-CC areas especially over the Arctic and most of the mid-latitude landmasses. This indicates that the expected increase in extreme precipitation over these regions does not follow the local warming at the CC rate. This result is consistent with the enhanced warming expected over these regions, while the surrounding oceans (the main source of moisture) are warming less quickly.

4. Discussion and conclusion

Despite an overall agreement that extreme precipitation follow a ≈7%/K rate of increase at the global scale, projected changes in extreme precipitation are influenced by multiple factors that can lead to large uncertainties at the regional scale. In this study, we quantify uncertainty in the projected changes in extreme precipitation — while most studies look at the mean or median change across an ensemble of models — using a single high-emission scenario. We provide a first assessment of the 10%–90% range in the extreme daily precipitation responses at the grid-point scale and a global picture of the regions where changes in extreme precipitation are consistent with the CC rate. Our results suggest that uncertainty is usually quite large. Averaged globally, GSAT scaling ranges extend from about 0 up to a super-CC rate, with a median close to the CC rate. Uncertainty can be larger if changes in extreme precipitation are investigated for a given GWL. This may be an artifact of internal variability due to the lack of sampling which has a stronger relative contribution at lower GWLs compared to our selected very-high emissions scenario.

Our assessed CMIP6 uncertainty arises both from model uncertainty and internal variability, as our calculations are based on single runs from each CMIP6 model. Internal variability can be seen as a basic sampling uncertainty, which could be overcome by averaging across multiple members for each global climate model. Model uncertainty alone would lead to narrower ranges than those reported in this study. However, despite the widening induced by a non-negligible contribution of internal variability, our results show that the intensification of extreme daily precipitation is robust over most regions, with more than 90% of models simulating an increase of 20-yr RVs. We believe that this study helps strengthen our confidence in the intensification of extreme precipitation.

Most regions around the world exhibit a RV20 change consistent with the CC rate of ≈7%/K. Remarkably, about 83% of the global land fraction is consistent with this rate of change when scaled by ΔGSAT. Exceptions to this include limited areas over subtropical oceans (showing a significantly sub-CC rate), and parts of the equatorial Pacific and Sahelian ITCZ (showing a significantly super-CC rate). These findings are consistent with well-known projected changes in large-scale atmospheric circulation, i.e., strengthened subsidence over the subtropics and enhanced convection over the core of the ITCZ (Douville et al., 2021). Not surprisingly, the rate of change in the Arctic is particularly sensitive to the scaling applied, since this region is warming much faster than the global average. This example suggests that the spatial distribution of the warming (e.g., Arctic amplification, land–sea contrast) can be also responsible for changes in the low-level atmospheric circulation and, therefore, for the departure from the CC rate of intensification.

Due to the uncertainty, the rate of change in extreme precipitation depicted here only represents a plausible scenario. This hints at the fact that we cannot produce a more accurate projection until we limit both model uncertainty and internal variability. Better filtering of internal variability would require using multiple ensemble members for each CMIP model — which are not available at the moment except for a few models. Therefore, we suggest to the modeling community to consider producing a minimum number (at least 9 according to O'Neill et al. (2016)) of realizations for each selected emissions scenario in the forthcoming CMIP7 exercise. Beyond internal variability, evidence suggests that modeling uncertainty also contributes to a large fraction

of the reported uncertainty. This source of uncertainty is related to our limited knowledge of the key physical processes controlling the response of extreme precipitation that is simulated by both global and regional climate models. Thus the generation of large ensembles along with other improvements like the development and wider use of convection-permitting models (Lucas-Picher et al., 2021) could increase the reliability of projected changes in extreme precipitation. Other methods such as the development and application of observational constraints (Ribes et al., 2021) could be also very useful to constrain the response of both global and regional climate models.

Declaration of competing interest

The authors declare that they have no known competing financial interests or personal relationships that could have appeared to influence the work reported in this paper.

Acknowledgments

This work is part of the Climate Advanced Forecasting of sub-seasonal Extremes (CAFE) project, which has received funding from the European Union's Horizon 2020 research and innovation program under the Marie Sklodowska-Curie grant agreement No 813844. We acknowledge the World Climate Research Programme's Working Group on Coupled Modelling, which is responsible for CMIP, and we thank the climate modeling groups for producing and making available their model output to CMIP. We also thank the Institut Pierre-Simon Laplace (ISPL) Mésocentre for Climate Sciences for the CMIP6 data acquisition, storage space, and intensive computing resources for this paper.

Appendix A. Supplementary data

Supplementary material related to this article can be found online at https://doi.org/10.1016/j.wace.2022.100435.

References

Alexander, L.V., Zhang, X., Peterson, T.C., Caesar, J., Gleason, B., Klein Tank, A., Haylock, M., Collins, D., Trewin, B., Rahimzadeh, F., et al., 2006. Global observed changes in daily climate extremes of temperature and precipitation. J. Geophys. Res.: Atmos. 111 (D5).

Allan, R.P., Soden, B.J., 2008. Atmospheric warming and the amplification of precipitation extremes. Science 321 (5895), 1481–1484.

Allen, M.R., Ingram, W.J., 2002. Constraints on future changes in climate and the hydrologic cycle. Nature 419 (6903), 228–232.

Arrhenius, S., 1896. Xxxi. on the influence of carbonic acid in the air upon the temperature of the ground. Lond. Edinb. Dublin Philos. Mag. J. Sci. 41 (251), 237–276.

Asadieh, B., Krakauer, N.Y., 2015. Global trends in extreme precipitation: climate models versus observations. Hydrol. Earth Syst. Sci. 19 (2), 877–891.

Bador, M., Donat, M.G., Geoffroy, O., Alexander, L.V., 2018. Assessing the robustness of future extreme precipitation intensification in the cmip5 ensemble. J. Clim. 31 (16), 6505–6525.

Berg, P., Haerter, J., Thejll, P., Piani, C., Hagemann, S., Christensen, J., 2009. Seasonal characteristics of the relationship between daily precipitation intensity and surface temperature. J. Geophys. Res.: Atmos. 114 (D18).

Chan, S.C., Kendon, E.J., Berthou, S., Fosser, G., Lewis, E., Fowler, H.J., 2020. Europe-wide precipitation projections at convection permitting scale with the unified model. Clim. Dynam. 55 (3), 409–428.

Cohen, J., Screen, J., Furtado, J., Barlow, M., Whittleston, D., Coumou, D., Francis, J., Dethloff, K., Entekhabi, D., Overland, J., et al., 2014. Recent arctic amplification and extreme mid-latitude weather. Nat. Geosci. 7, 627–637.

Coles, S., Bawa, J., Trenner, L., Dorazio, P., 2001. An Introduction to Statistical Modeling of Extreme Values, Vol. 208. Springer.

Cooley, D., Nychka, D., Naveau, P., 2007. Bayesian spatial modeling of extreme precipitation return levels. J. Amer. Statist. Assoc. 102 (479), 824–840.

Douville, H., John, A., 2021. Fast adjustment versus slow sst-mediated response of daily precipitation statistics to abrupt 4xco 2. Clim. Dynam. 56 (3), 1083–1104.

Douville, H., Raghavan, K., Renwick, J., Allan, R., Arias, P., Barlow, M., Cerezo-Mota, R., Cherchi, A., Gan, T., Gergis, J., Jiang, D., Khan, A., Pokam Mba, W., Rosenfeld, D., Tierney, J., Zolina, O., 2021. Water cycle changes. In: Masson-Delmotte, V., Zhai, P., Pirani, A., Connors, S.L., Péan, C., Berger, S., Caud, N., Chen, Y., Goldfarb, L., Gomis, M.I., Huang, M., Leitzell, K., Lonnoy, E., Matthews, J.B.R., Maycock, T.K., Waterfield, T., Yelekçi, O., Yu, R., Zhou, B. (Eds.), Climate Change 2021: The Physical Science Basis. Contribution of Working Group I to the Sixth Assessment Report of the Intergovernmental Panel on Climate Change. Cambridge University Press, chapter 11 (in press).

Easterling, D.R., Kunkel, K.E., Wehner, M.F., Sun, L., 2016. Detection and attribution of climate extremes in the observed record. Weather Clim. Extremes 11, 17–27.

Eyring, V., Bony, S., Meehl, G.A., Senior, C.A., Stevens, B., Stouffer, R.J., Taylor, K.E., 2016. Overview of the coupled model intercomparison project phase 6 (cmip6) experimental design and organization. Geosci. Model Dev. 9 (5), 1937–1958.

Hardwick Jones, R., Westra, S., Sharma, A., 2010. Observed relationships between extreme sub-daily precipitation, surface temperature, and relative humidity. Geophys. Res. Lett. 37 (22).

Kao, S.-C., Ganguly, A.R., 2011. Intensity, duration, and frequency of precipitation extremes under 21st-century warming scenarios. J. Geophys. Res.: Atmos. 116 (D16).

Karl, T.R., Easterling, D.R., 1999. Climate extremes: Selected review and future research directions. Clim. Change 42 (1), 309–325.

Karl, T.R., Nicholls, N., Ghazi, A., 1999. Clivar/gcos/wmo workshop on indices and indicators for climate extremes workshop summary. Weather Clim. Extremes 3–7, Springer.

Kharin, V.V., Zwiers, F.W., Zhang, X., Hegerl, G.C., 2007. Changes in temperature and precipitation extremes in the ipcc ensemble of global coupled model simulations. J. Clim. 20 (8), 1419–1444.

Kharin, V.V., Zwiers, F., Zhang, X., Wehner, M., 2013. Changes in temperature and precipitation extremes in the cmip5 ensemble. Clim. Change 119 (2), 345–357.

Knutti, R., Masson, D., D. & a. gettelman (2013), 2013. Climate Model Genealogy: Generation CMIP5 and how We Got There. pp. 1194–1199.

Lee, J., Marotzke, J., Bala, G., Cao, L., Corti, S., Dunne, J., Engelbrecht, F., Fischer, E., Fyfe, J., Jones, C., et al., 2021. Future global climate: scenariobased projections and near-term information. Clim. Change.

Lehner, F., Deser, C., Maher, N., Marotzke, J., Fischer, E.M., Brunner, L., Knutti, R., Hawkins, E., 2020. Partitioning climate projection uncertainty with multiple large ensembles and cmip5/6. Earth Syst. Dyn. 11 (2), 491–508.

Li, C., Zwiers, F., Zhang, X., Li, G., Sun, Y., Wehner, M., 2020. Changes in annual extremes of daily temperature and precipitation in cmip6 models. J. Clim. 1–61.

Lucas-Picher, P., Argüeso, D., Brisson, E., Tramblay, Y., Berg, P., Lemonsu, A., Kotlarski, S., Caillaud, C., 2021. Convection-permitting modeling with regional climate models: Latest developments and next steps. Wiley Interdiscip. Rev. Clim. Change e731.

Masson-Delmotte, V., Zhai, P., Pirani, A., Connors, S.L., Péan, C., Berger, S., Caud, N., Chen, Y., Goldfarb, L., Gomis, M.I., Huang, M., Leitzell, K., Lonnoy, E., Matthews, J.B.R., Maycock, T.K., Waterfield, T., Yelekçi, O., Yu, R., Zhou, B. (Eds.), 2021. Ipcc, 2021: Summary for policymakers. Climate Change 2021: The Physical Science Basis. Contribution of Working Group I to the Sixth Assessment Report of the Intergovernmental Panel on Climate Change. Cambridge University Press, (in press).

Min, S.-K., Zhang, X., Zwiers, F.W., Hegerl, G.C., 2011. Human contribution to more-intense precipitation extremes. Nature 470 (7334), 378–381.

Mizuta, R., Endo, H., 2020. Projected changes in extreme precipitation in a 60-km agcm large ensemble and their dependence on return periods. Geophys. Res. Lett. 47 (13), e2019GL086855.

Muller, C.J., O'Gorman, P.A., Back, L.E., 2011. Intensification of precipitation extremes with warming in a cloud-resolving model. J. Clim. 24 (11), 2784–2800.

Nath, R., Luo, Y., Chen, W., Cui, X., 2018. On the contribution of internal variability and external forcing factors to the cooling trend over the humid subtropical indo-gangetic plain in india. Sci. Rep. 8 (1), 1–11.

O'Gorman, P.A., 2015. Precipitation extremes under climate change. Curr. Clim. Change Rep. 1 (2), 49–59.

O'Neill, B.C., Tebaldi, C., v. Vuuren, D.P., Eyring, V., Friedlingstein, P., Hurtt, G., Knutti, R., Kriegler, E., Lamarque, J.-F., Lowe, J., et al., 2016. The scenario model intercomparison project (scenariomip) for cmip6. Geosci. Model Dev. 9 (9), 3461–3482.

Pall, P., Allen, M., Stone, D.A., 2007. Testing the clausius–clapeyron constraint on changes in extreme precipitation under co 2 warming. Clim. Dynam. 28 (4), 351–363.

Pall, P., Patricola, C.M., Wehner, M.F., Stone, D.A., Paciorek, C.J., Collins, W.D., 2017. Diagnosing conditional anthropogenic contributions to heavy colorado rainfall in september 2013. Weather Clim. Extremes 17, 1–6.

Pendergrass, A., Coleman, D., Deser, C., Lehner, F., Rosenbloom, N., Simpson, I., 2019. Nonlinear response of extreme precipitation to warming in cesm1. Geophys. Res. Lett. 46 (17–18), 10551–10560.

Peterson, T., Folland, C., Gruza, G., Hogg, W., Mokssit, A., Plummer, N., 2001. Report on the Activities of the Working Group on Climate Change Detection and Related Rapporteurs. Citeseer.

Pfahl, S., O'Gorman, P.A., Fischer, E.M., 2017. Understanding the regional pattern of projected future changes in extreme precipitation. Nature Clim. Change 7 (6), 423–427.

Ribes, A., Qasmi, S., Gillett, N.P., 2021. Making climate projections conditional on historical observations. Sci. Adv. 7 (4), eabc0671.

Scherrer, S.C., Fischer, E.M., Posselt, R., Liniger, M.A., Croci-Maspoli, M., Knutti, R., 2016. Emerging trends in heavy precipitation and hot temperature extremes in switzerland. J. Geophys. Res.: Atmos. 121 (6), 2626–2637.

Schroeer, K., Kirchengast, G., 2018. Sensitivity of extreme precipitation to temperature: the variability of scaling factors from a regional to local perspective. Clim. Dynam. 50 (11), 3981–3994.

Seneviratne, S.I., 2012. Historical drought trends revisited. Nature 491 (7424), 338–339.

Seneviratne, S., Zhang, X., Adnan, M., Badi, W., Dereczynski, C., Di Luca, A., Ghosh, S., Iskandar, I., Kossin, J., Lewis, S., Otto, F., Pinto, I., Satoh, M., Vicente-Serrano, S.M., Wehner, M., Zhou, B., 2021. Weather and climate extreme events in a changing climate. In: Masson-Delmotte, V., Zhai, P., Pirani, A., Connors, S.L., Péan, C., Berger, S., Caud, N., Chen, Y., Goldfarb, L., Gomis, M.I., Huang, M., Leitzell, K., Lonnoy, E., Matthews, J.B.R., Maycock, T.K., Waterfield, T., Yelekçi, O., Yu, R., Zhou, B. (Eds.), Climate Change 2021: The Physical Science Basis. Contribution of Working Group I to the Sixth Assessment Report of the Intergovernmental Panel on Climate Change. Cambridge University Press, chapter 11 (in press).

Sherwood, S., Roca, R., Weckwerth, T., Andronova, N., 2010. Tropospheric water vapor, convection, and climate. Rev. Geophys. 48 (2).

Sillmann, J., Kharin, V., Zhang, X., Zwiers, F., Bronaugh, D., 2013a. Climate extremes indices in the cmip5 multimodel ensemble: Part 1. model evaluation in the present climate. J. Geophys. Res.: Atmos. 118 (4), 1716–1733.

Sillmann, J., Kharin, V.V., Zwiers, F., Zhang, X., Bronaugh, D., 2013b. Climate extremes indices in the cmip5 multimodel ensemble: Part 2. future climate projections. J. Geophys. Res.: Atmos. 118 (6), 2473–2493.

Sugiyama, M., Shiogama, H., Emori, S., 2010. Precipitation extreme changes exceeding moisture content increases in miroc and ipcc climate models. Proc. Natl. Acad. Sci. 107 (2), 571–575.

Sun, Q., Zhang, X., Zwiers, F., Westra, S., Alexander, L.V., 2021. A global, continental, and regional analysis of changes in extreme precipitation. J. Clim. 34 (1), 243–258.

Swart, N.C., Cole, J.N., Kharin, V.V., Lazare, M., Scinocca, J.F., Gillett, N.P., Anstey, J., Arora, V., Christian, J.R., Hanna, S., et al., 2019. The canadian earth system model version 5 (canesm5. 0.3). Geosci. Model Dev. 12 (11), 4823–4873.

Tebaldi, C., Hayhoe, K., Arblaster, J.M., Meehl, G.A., 2006. Going to the extremes. Clim. Change 79 (3), 185–211.

Trenberth, K.E., 2011. Changes in precipitation with climate change. Clim. Res. 47 (1–2), 123–138.

Utsumi, N., Seto, S., Kanae, S., Maeda, E.E., Oki, T., 2011. Does higher surface temperature intensify extreme precipitation? Geophys. Res. Lett. 38 (16).

Vial, J., Dufresne, J.-L., Bony, S., 2013. On the interpretation of inter-model spread in cmip5 climate sensitivity estimates. Clim. Dynam. 41 (11–12), 3339–3362.

Wang, G., Wang, D., Trenberth, K.E., Erfanian, A., Yu, M., Bosilovich, M.G., Parr, D.T., 2017. The peak structure and future changes of the relationships between extreme precipitation and temperature. Nature Clim. Change 7 (4), 268–274.

Wehner, M.F., 2020. Characterization of long period return values of extreme daily temperature and precipitation in the cmip6 models: Part 2, projections of future change. Weather Clim. Extremes 30, 100284.

Wehner, M., Gleckler, P., Lee, J., 2020. Characterization of long period return values of extreme daily temperature and precipitation in the cmip6 models: Part 1, model evaluation. Weather Clim. Extremes 30, 100283.

Westra, S., Alexander, L.V., Zwiers, F.W., 2013. Global increasing trends in annual maximum daily precipitation. J. Clim. 26 (11), 3904–3918.

Wyser, K., Noije, T.v., Yang, S., v. Hardenberg, J., O'Donnell, D., Döscher, R., 2020. On the increased climate sensitivity in the ec-earth model from cmip5 to cmip6. Geosci. Model Dev. 13 (8), 3465–3474.

Zelinka, M.D., Myers, T.A., McCoy, D.T., Po-Chedley, S., Caldwell, P.M., Ceppi, P., Klein, S.A., Taylor, K.E., 2020. Causes of higher climate sensitivity in cmip6 models. Geophys. Res. Lett. 47 (1), e2019GL085782.

Zhang, W., Villarini, G., Wehner, M., 2019. Contrasting the responses of extreme precipitation to changes in surface air and dew point temperatures. Clim. Change 154 (1), 257–271.